Results in Physics 14 (2019) 102461

Contents lists available at ScienceDirect

Results in Physics

journal homepage: www.elsevier.com/locate/rinp

A triple-band terahertz metamaterial absorber based on buck Dirac semimetals

Weiwei Meng[a], Longcheng Que[a,*], Jian Lv[a,*], Liwei Zhang[b], Yun Zhou[a], Yadong Jiang[a]

[a] State Key Laboratory of Electronic Thin Film and Integrated Devices, University of Electronic Science and Technology of China, Chengdu 610054, China
[b] School of Physics & Electronic Information Engineering, Henan Polytechnic University, Jiaozuo 454000, China

ARTICLE INFO

Keywords:
BDSs
Terahertz
Perfect absorber
Polarization-independent

ABSTRACT

In this paper, a triple-band terahertz metamaterial absorber (MA) based on buck Dirac semimetals (BDSs) is proposed, which consists of a windmill-shaped element in a square ring layer, a dielectric layer, and a BDSs layer. The MA unit cell is investigated at normal and oblique incidence angle for both transverse electric (TE) and transverse magnetic (TM) polarizations. The simulation results show that the MA has three high absorption peaks at 0.80 THz, 1.72 THz, and 3.38 THz. The corresponding peak absorbance are 99.43%, 99.92% and 99.58%, respectively. Moreover, the absorption peaks of MA can be tuned by adjusting the Fermi energy of the BDSs. And the density of electric field, the magnetic field, and surface current distributions of the MA are given to reveal the absorption mechanism. According to the simulation results, the designed MA not only has high absorbance, but also insensitive to polarizations. Hence it is favorable for various applications, such as terahertz detecting, radar stealth and bio-chemical sensor.

Introduction

Metamaterial absorbers (MAs) is a kind of subwavelength periodic material which is designed and manufactured manually. In 2008 years, Landy et al [1] first proposed and demonstrated a kind of single-band MA, which has a near unit of absorbance. Subsequently, the scholars from all over the world began to do research on MAs and metasurfaces [2,3], mainly involving broadband and narrow-band MAs from microwave [4,5], terahertz wave [6–8], infrared wave [9] to visible light [10,11]. The MAs have widely potential applications in many fields, such as electromagnetic cloaking [12], electromagnetic absorption [13], sensor [14], solar cell [15], stealth [16] and so on. In the study of MAs, theory of transmission lines, multi-reflection interference theory and impedance matching are used to analyze and design the MAs, qualitatively. Then, the finite element simulation software is usually adopted to design and optimize the structure of MA. After that, the designed MA will be verified through experiments.

Generally, there are two kinds of design methods to achieve multi-bandwidth MA, one is to place multiple absorption units with different resonant frequencies on the same plane of the MA unit, and the other is to place absorption units with different resonant frequencies on different planes. However, the first method will cause the size of the MA unit to be large, which will shadow the scene of its application. The second way will increase the difficulty of fabrication processing. Although, many non-tunable one-bandwidth, dual-bandwidth and triple-band of MAs [17,18] have been reported, the triple-band MAs are rarely reported. Moreover, the MAs designed with traditional metal material (such as gold and silver) have fixed absorption spectrum, and the absorption spectrum of the MAs cannot be tuned unless the geometry of the MAs is carefully optimized.

Bulk Dirac semimetals (BDSs) is a kind of novel state three-dimensional (3D) quantum material (such as Cd_3As_2, Na_3Bi, etc.) [19,20], and the electronic band structures of BDSs has linear dispersion characteristics in the 3D momentum space direction. The permittivity functions of BDSs can be dynamically tuned by changing its Fermi level (E_F) through alkaline surface doping or bias voltage [21,22]. The BDSs has ultra-high mobility, high magneto resistance, and other exotic electrical and optical properties, therefore, the BDSs also called “3D graphene”. The BDSs has attracted great interests among international scholars.

Comparing to monoatomic layer graphene material, the BDSs materials are more stable against environmental conditions and technological factors changes. What’s more, the carrier mobility of BDSs is much higher than graphene, for the crystalline symmetry prevention against gap formation in BDSs [23]. The BDSs has very-high electron mobility up to 9×10^6 cm^2 V^{-1} s^{-1} at 5 K [24], and the electron mobility of graphene is 2×10^5 cm^2 V^{-1} s^{-1} at 5 K [25], merely. Because of the excellent properties of BDSs, it has potentially applications in many fields, such as photonics and plasmonic. In recent years, many

* Corresponding authors.
E-mail addresses: lcque@uestc.edu.cn (L. Que), lvjian@uestc.edu.cn (J. Lv).

https://doi.org/10.1016/j.rinp.2019.102461
Received 16 April 2019; Received in revised form 3 June 2019; Accepted 18 June 2019
Available online 28 June 2019

scholars have reported some research results based on BDSs in tunable MA [26,27], plasmon-induced transparency (EIT) [28], and so on.

The BDSs show a metallic response at frequencies lower than Fermi energy, and a dielectric response becomes dominated at higher frequencies. Because the BDSs shows metallic property at the THz frequencies, so it may be more convenient than graphene to design a tunable MA for the BDSs, which can be served as reflection layer of MA.

In this paper, a triple-band terahertz MA based on BDSs is presented, which consists of a windmill-shaped element in a square ring layer, a dielectric layer and a BDSs layer. The MA unit cell is investigated at normal and oblique incidence angles for both TE and TM polarizations. The simulation results show that the MA has three high absorption peaks (greater than 99%), and the absorption peaks can be tuned by adjusting the E_F of BDSs. The density of electric field, magnetic field and surface current distributions of the MA are given to reveal the absorption mechanism. Furthermore, numerical simulation is performed to explain the relationship of the absorbance and the thickness of dielectric, incidence angle, E_F, and the imaginary part k of dielectric.

Structure design and simulation

The schematic structure of proposed MA and the direction of TE/TM polarizations incident wave are illustrated in Fig. 1. The finite element method based on commercial software COMSOL Multiphysics 5.3a [29] is used to optimize the structure of MA, and the geometry parameters of MA are shown as in Table 1. The absorption layer is gold, whose conductivity is $\delta = 4.56 \times 10^7$ S/m and the thickness (h_{12}) is 0.2 μm. The thickness (h_1) of the BDSs layer is set to 20 μm, which is enough to make sure BDSs layer is opaque. Hence, the transmission of the MA is totally eliminated, and the dynamic conductivity of BDSs is described with Eqs. (1) and (2). The polyimide is selected as dielectric layer of MA, and the refractive index (RI) and thickness (h_2) are n = 3*(1 + 0.06*i) [30] and 8 μm, respectively.

In order to make the MA unit cell equivalent to periodic array, the MA unit cell boundary and ports are set as Floquet periodic boundary and periodic ports, respectively, as shown in Fig. 1(a). The absorption spectrum of MA can be written as 1-R(ω)-T(ω) = 1-$|S_{11}|^2$-$|S_{21}|^2$ [31]. In this paper, the absorption spectrum of MA becomes A(ω) = 1-R(ω) = 1-$|S_{11}|^2$, for the existence of BDSs layer.

The dynamic conductivity of the BDSs is obtained by using the Kubo formalism in random-phase approximation theory at the long-wavelength limit. The real and imaginary parts of dynamic conductivity of the BDSs can be expressed as [32]:

$$\mathrm{Re}\,\sigma(\Omega) = \frac{e^2}{\hbar}\frac{gk_F}{24\pi}\Omega G(\Omega/2) \tag{1}$$

Table 1
The geometry parameters of MA.

W/L	D	D_1	D_2	D_3
70 μm	6 μm	14.75 μm	26.5 μm	4 μm

$$\mathrm{Im}\sigma(\Omega) = \frac{e^2}{\hbar}\frac{gk_F}{24\pi}\left[\frac{4}{\Omega}\left(1+\frac{\pi^2}{3}\left(\frac{T}{E_F}\right)^2\right) + 8\Omega\int_0^{\varepsilon_c}\left(\frac{G(\varepsilon)-G(\Omega-2)}{\Omega^2-4\varepsilon^2}\right)\varepsilon d\varepsilon\right] \tag{2}$$

where G(E) = n(-E)-n(E), n(E) is the Fermi distribution function, $k_F = E_F/\hbar\nu_F$ is the Fermi momentum, E_F is the Fermi level, $\nu_F = 10^6$m/s is the Fermi velocity, $\Omega = \hbar\omega/E_F$, $\varepsilon = E/E_F$, $\varepsilon_c = E_c/E_F$ (Ec = 3 is the cutoff energy beyond which the Dirac spectrum is no longer linear), e is the electron charge, and g is the degeneracy actor (g = 4 for Na_3Bi or Cd_3As_2).

According to Eqs. (1) and (2), we calculated the σ(Ω) of the BDSs as shown in Fig. 2. The real (a) and the imaginary (b) parts of the σ(Ω) are as a function of the normalized frequency $\Omega = \hbar\omega/E_F$, where g = 4, $\varepsilon_c = 3$ and $\nu_F = 10^6$m/s. As shows in Fig. 2(a). When the Ω is less-than 2, the real parts of the σ(Ω) is equal to 0 and a leaping increase appears at Ω = 2. The imaginary parts of σ(Ω) intersect at one point at Ω = 1.23, and at Ω = 2 the imaginary parts of σ(Ω) has a undershoot.

Fig. 3 shows the permittivity of the BDSs, it is obviously that the permittivity of the BDSs is very sensitive to the Fermi level E_F. As the E_F increases, both the real and imaginary parts of the permittivity are dramatically increase. The dynamic conductivity of the BDSs has two parts, one is interband conductivity and other is intraband conductivity. For the one-band mode, it can be considered as the interband conductivity, so the permittivity (ε) of the BDSs is obtained as follows [33]:

$$\varepsilon = \varepsilon_b + i\sigma/\omega\varepsilon_0 \tag{3}$$

where ε_b is the effective dielectric constant of background and ε_0 is the permittivity of vacuum. For Cd_3As_2 or Na_3Bi, $\varepsilon_b = 13$, and this value will be used in the following calculations.

According to the theory of transmission line, the equivalent circuit model [34,35] of the proposed MA is extracted and presented in Fig. 4. In the structure of proposed MA, the BDSs layer is placed at the back of the MA to ensure the zero transmission. In the analysis of transmission line model, the BDSs layer can be regarded as a short-circuit device because of its zero characteristic impedance.

Fig. 4(a) shows the parasitic parameters of the MA, it is clearly that the MA has three LC loops. Therefore, the MA has three absorption peaks, and the general equivalent circuit model of MA is depicted in

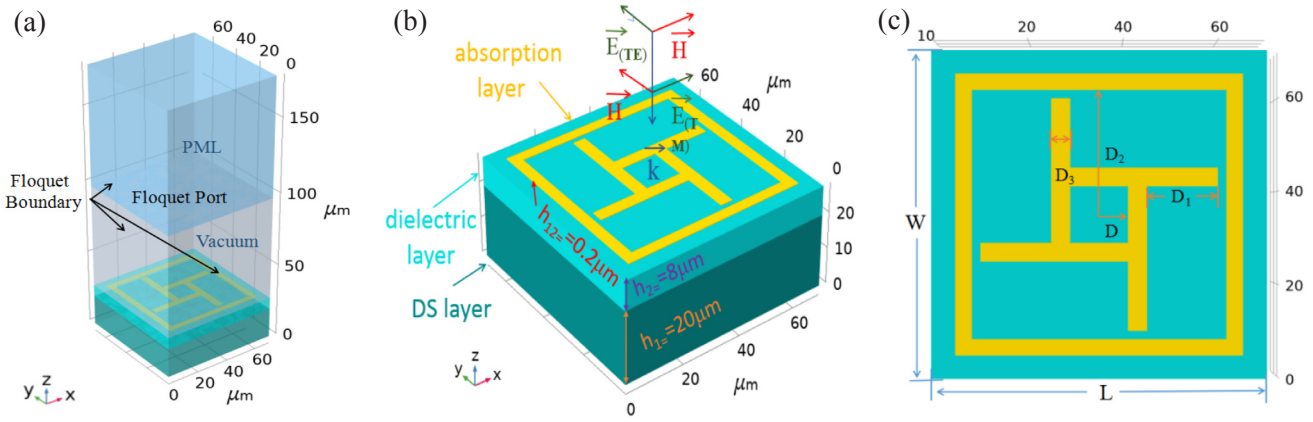

Fig. 1. The schematic diagram of proposed MA unit cell: (a) periodic structure of MA, (b) perspective view (with TE/TM polarizations direction along x/y axis), (c) top view.

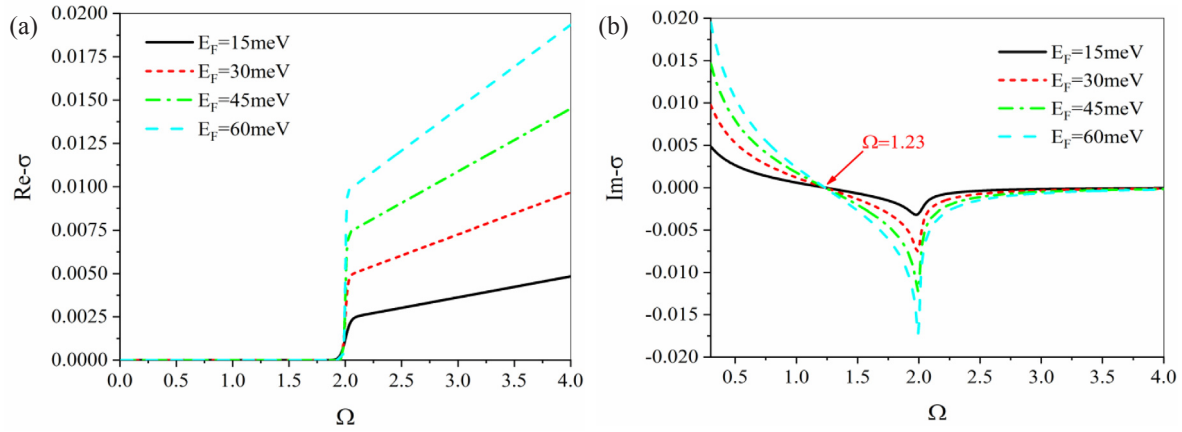

Fig. 2. The real (a) and the imaginary (b) parts of the σ(Ω) are as a function of the normalized frequency $\Omega = \hbar\omega/E_F$ at different E_F.

Fig. 4(b). The impedance Z_{AL} of absorption layer can be expressed as:

$$Z_{AL} = \frac{Z_1 Z_2 Z_3}{Z_1 Z_2 + Z_1 Z_3 + Z_2 Z_3} \tag{4}$$

$$Z_i = \frac{(1 + sR_{ii}C_i)(R_i + sL_i) + R_{ii}}{1 + sR_{ii}C_i} \tag{5}$$

where $s = j\omega$; $\omega = 2\pi f$; $i = 1, 2, 3$.

The impedance Z_d of dielectric layer with thickness h_2 can be written as follows,

$$Z_d = i\frac{\eta_0}{\sqrt{\varepsilon_r}}\tan(k_0 h_2\sqrt{\varepsilon_r}) = i\eta_d \tan(k_0 h_2\sqrt{\varepsilon_r}) \tag{6}$$

where η_0 is free space characteristic impedance, k_0 is wavenumber, and d is the dielectric thickness.

Based on the calculation of Z_{AL} and Z_d, the impedance Z_{in} of MA can be computed by the relation below,

$$Z_{in} = \frac{Z_{AL} Z_d}{Z_{AL} + Z_d} \tag{7}$$

Finally, the reflectance (R(ω)) is yielded by (8),

$$R(\omega) = \frac{Z_{in} - Z_0}{Z_{in} + Z_0} \tag{8}$$

When the input impedance (Z_{in}) of MA matches with the free space characteristic impedance (Z_0), the reflectance of MA become to be zero.

The equivalent circuit components shown in Table 2 are calculated by using the geometry parameters shown in Table 1. The equivalent circuit model of the MA is simulated by using the PSPICE, and Fig. 5. shows the simulation results of PSPICE and COMSOL. It is obvious that the equivalent circuit absorption spectrum of MA has good consistent with COMSOL. The simulation results indicate that the extracted equivalent circuit model is very effective for the proposed MA.

Results and discussion

For the sake of illustrating the performance and operating principle of the proposed MA, the optical response, effective impedance, the density of electric field, magnetic field and surface current of the proposed MA are presented. The TE and TM polarizations absorption spectrum of MA are provided in Fig. 6(a). The presented MA has three high absorption peaks at 0.8 THz, 1.72 THz and 3.38 THz, and the corresponding absorbance are 99.43% 99.92% 99.58%, respectively. Significantly, under the TE and TM polarizations absorption spectrum of MA are almost identical, which means the presented MA is not sensitive to incident TE and TM polarizations electromagnetic wave. The designed tunable triple-band MA's structure has symmetry on the x axis and y axis, therefore, the MA is not sensitive to incident TE and TM polarizations electromagnetic wave.

According to the theory of transmission line, the effective impedance of MA can be extracted from S parameters. Fig. 6(b). shows the effective impedance of MA, the red line and green line are the real part and imaginary part of the impedance of MA, respectively. On the basis of the principle of impedance match theory, when the effective impedance of the MA matches the intrinsic impedance of the vacuum, the reflectance (R(ω)) of the MA will be going to be zero. Therefore, the A(ω) of MA is going to be close to 1. The impedance equation [36] is expressed as

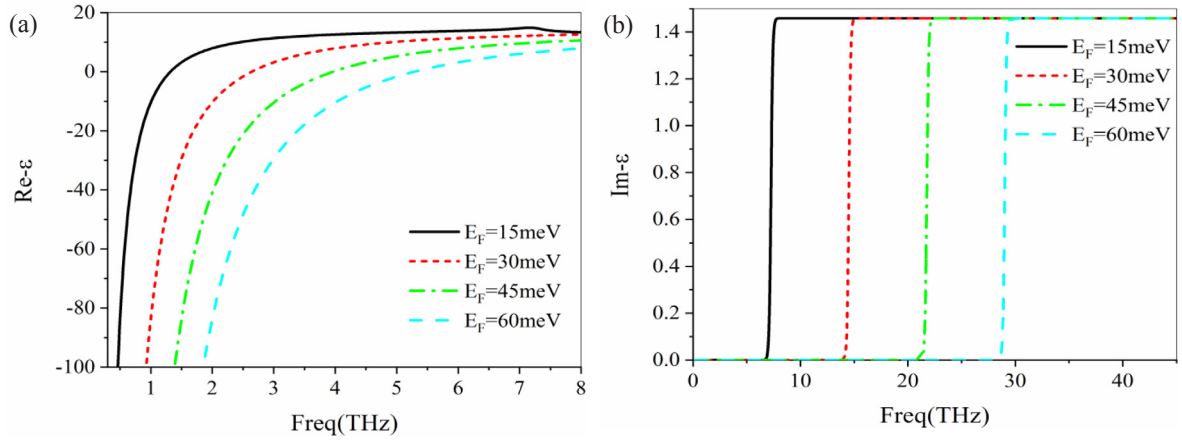

Fig. 3. The real (a) and the imaginary (b) parts of the permittivity of the BDSs at different E_F.

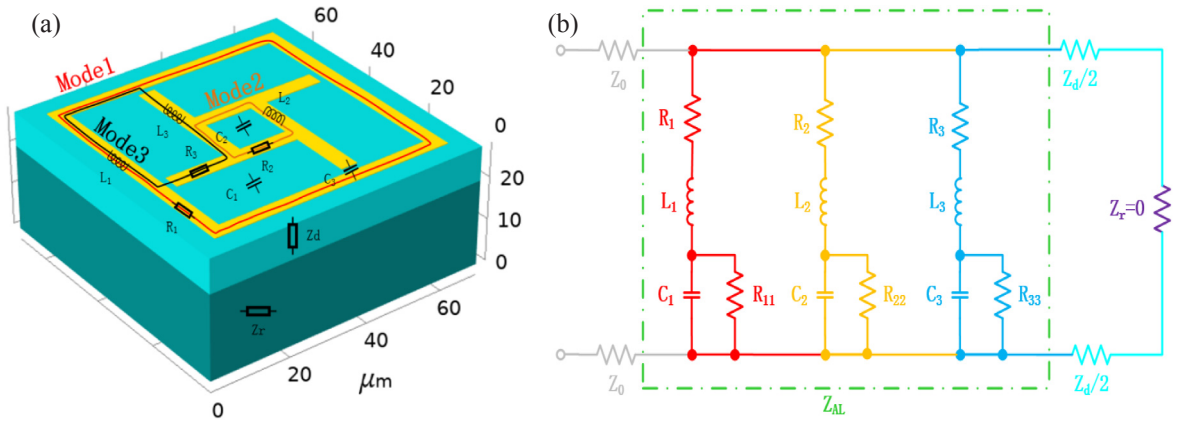

Fig. 4. (a). The structure of proposed MA, (b) the equivalent circuit model of MA.

Table 2
The equivalent circuit components (R, L, and C) values of MA.

Parameters	Value	Parameters	Value
R_1	265 Ω	L_1	14.52 pH
R_2	151 Ω	L_2	6.48 pH
R_3	79 Ω	L_3	3.48 pH
C_1	14.52 aF	R_{11}	8.31 MΩ
C_2	6.4 aF	R_{22}	6.27 MΩ
C_3	3.48 aF	R_{33}	3.72 MΩ

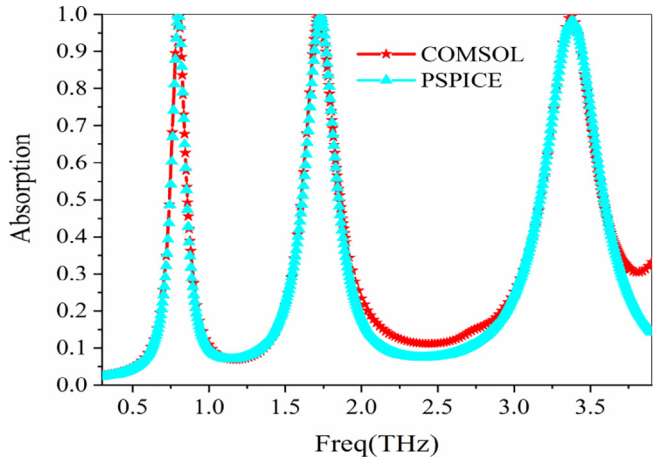

Fig. 5. Comparison of the simulation results between PSPICE and COMSOL.

$$Z(\omega) = \sqrt{\mu(\omega)/\varepsilon(\omega)} = \sqrt{\frac{(1+S_{11})^2 - S_{21}^2}{(1-S_{11})^2 - S_{21}^2}} \quad (9)$$

herein, the S_{21} and S_{11} represents the transmission and reflection coefficient, respectively.

As shown in Fig. 6(a) the absorption peaks of MA is distributed at 0.80 THz, 1.72 THz and 3.38 THz, respectively. Comparing Fig. 6(a) and (b) the absorption peaks of MA happens when the magnitude effective impedance is closed to 1, and the phenomenon also verified the validity of impedance matching theory.

In order to reveal the mechanism of MA has multi-band and high absorbance, the density of electric field, magnetic field and surface current (with arrows) distributions of MA at 0.80 THz, 1.72 THz and 3.38 THz are provided in Fig. 7. In Fig. 7 we can observe the excitation of the electric dipole on the ring: in mode 1, charges of opposite signs accumulate at the top and bottom ends of the outer ring and the electric field is mainly distributed at the upper and lower ends of the outer ring. The density of magnetic field and surface current have the same distribution on both sides of the ring.

From analyzing the distributions of the electric field, magnetic field and surface currents density, the electric dipole resonant mode of the MA is distinguished: 0.80 THz corresponds to the outer ring's resonance frequency, 1.72 THz corresponds to the windmill-shaped elements resonance frequency and 3.38 THz corresponds to the secondary resonant frequency of large ring and windmill-shaped elements. The high strength electric dipole resonance results in the high absorbance of MA. It should be mentioned that the mode of electric dipole corresponds to the three loops of the LC equivalent circuit.

The LC circuit model can be used to explain the resonant mode of

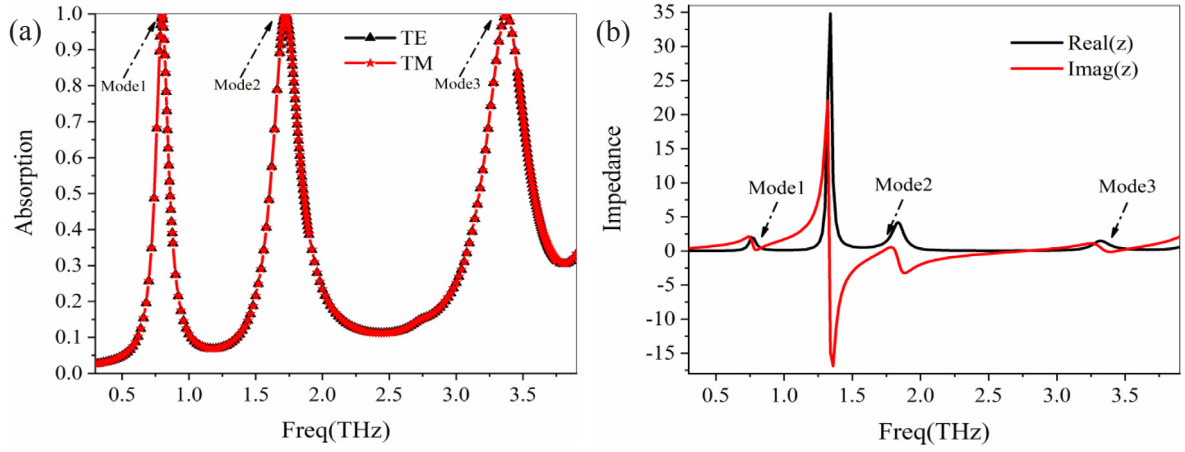

Fig. 6. (a) The absorption spectrum of MA at TE/TM polarizations, (b) The extracted effective impedance of the proposed MA.

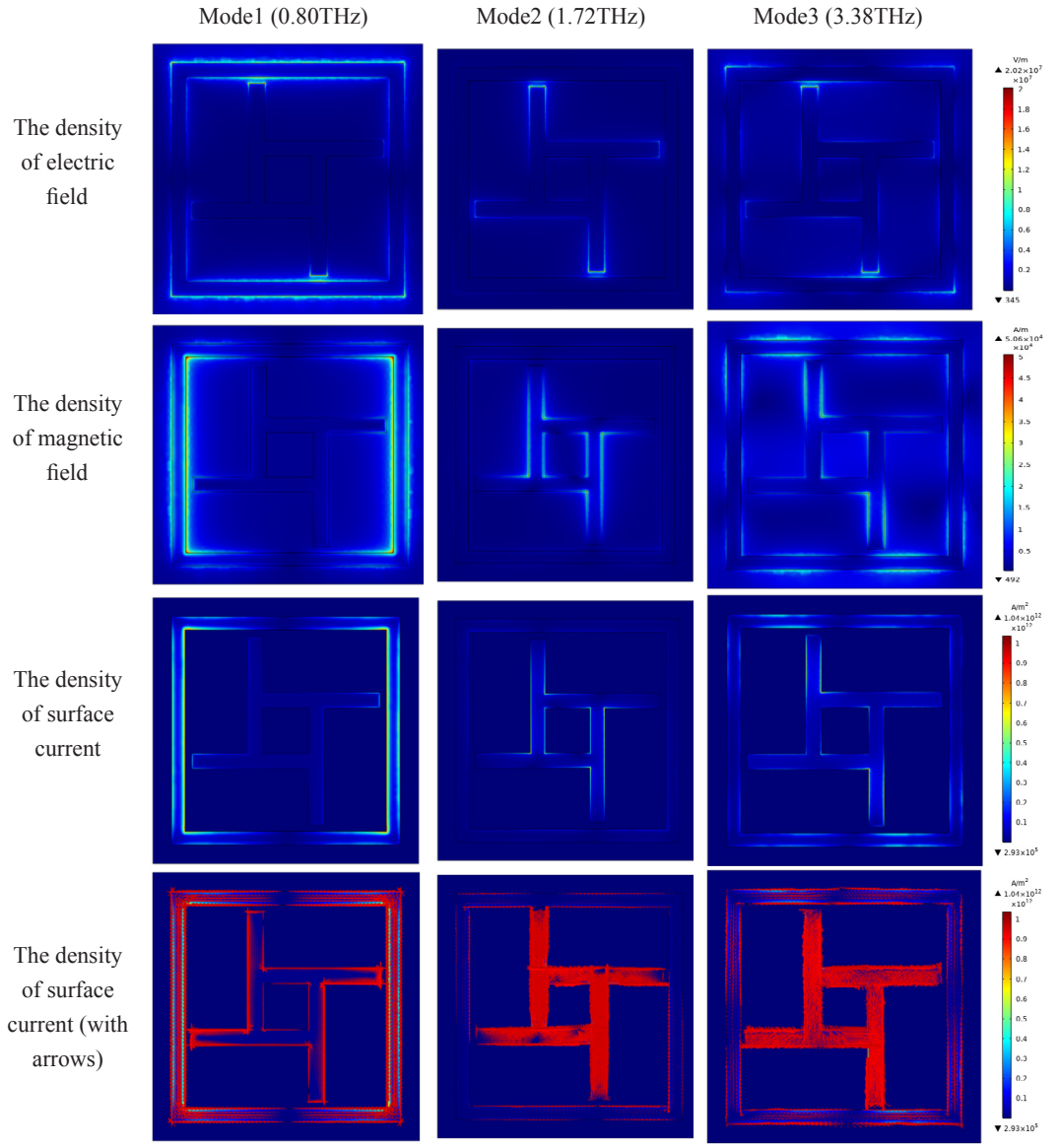

Fig. 7. The density of electric field, magnetic field and surface current distributions of the three absorption peaks of the MA.

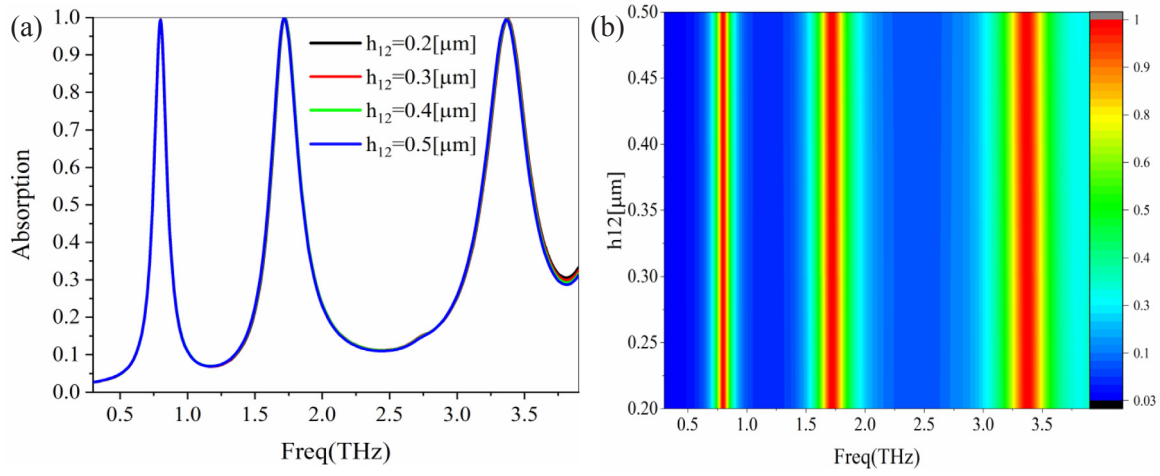

Fig. 8. (a) The absorption spectrum for different thickness of the absorption layer, (b) The scanning absorption spectrum under different thickness of absorption layer.

MA, and the potential resonant frequency of MA can be obtained by analyzing the equivalent resonance loop of MA. The resonant frequency equation is as follows [30]

$$f = \frac{1}{2\pi\sqrt{LC|_2}} \propto \frac{1}{L} \tag{10}$$

where C and L is the total parasitic capacitance and inductance of equivalent resonance loop, respectively. Eq. (10) suggests that the resonant frequency (f) of MA is inversely proportional to the parasitic C and L of equivalent resonance loop.

The three resonant modes of MA corresponding to the three absorption peaks of absorption spectrum. Fig. 7. shows that the density of electric field, magnetic field and surface current (with arrows) distributions of each resonant modes of MA, and with the frequency increasing the density of electric field, magnetic field and surface current distributions change from the outer large ring to the windmill-shaped element to the large ring and windmill-shaped element.

We have further investigated the effects of the MA's parameters on the stability of absorption spectrum of the MA, such as: the thickness of dielectric layer and absorption layer, the changes in the polarization angle, etc. The effect of absorption layer thickness (h_{12}) on the MA absorption spectrum is shown as Fig. 8. The thickness of absorption layer is increasing from 0.2[μm] to 0.5[μm], and the absorbance and the frequency of three absorption peaks almost have no change. It means that the thickness of the absorption layer almost does not affect the stability of the MA. Fig. 8(b) provided the scanning absorption spectrum under different thickness of absorption layer.

Fig. 9 offered the absorption spectrum under different thickness of dielectric layer (h_2), the thickness of dielectric layer changed from 7.6[μm] to 8.4[μm]. It can be clearly seen from Fig. 9(a) that the absorbance of MA is always close to 1 with the increasing of the thickness of dielectric layer, and the first two absorption peaks are hardly affected by the thickness of dielectric layer, but the third absorption peak has a slight change (red-shift). Fig. 9(b) provided the scanning absorption spectrum in different thickness of dielectric layer.

We also investigated the absorption stability of the MA under the changes of incident angle. At the normal incidence, the incidence electromagnetic wave along the z direction is 0°. Fig. 10. offered the scanning absorption spectrum with the incident angle from 0° to 60° in TE and TM polarizations. We note that the three absorption peaks of MA are closed to 1 in the normal incidence, and the first two absorption peaks maximum absorbance decreases slightly with the angle increasing. However, the third absorption peak appear some sonant wavelength and maximum absorbance decreases along with the incident angle increasing. The designed triple-band MA's structure has

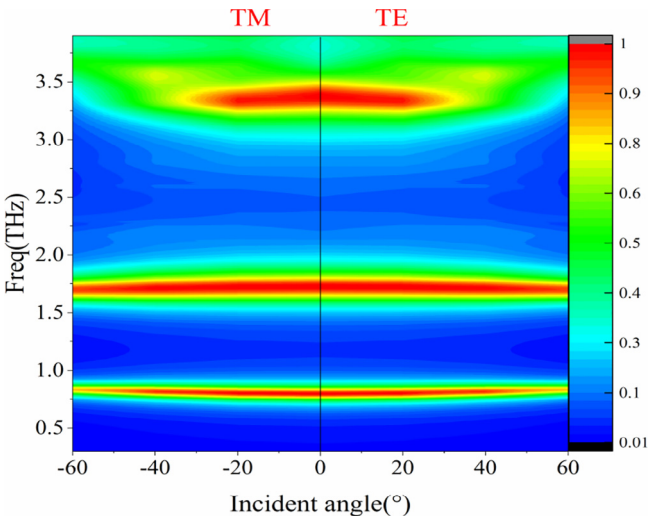

Fig. 10. The simulation scanning absorption spectrum with different incident angles under TE/TM polarizations.

symmetry on the x axis and y axis, therefore, the MA has wide incident angles absorbance for TE and TM polarizations.

According to the public reports, most of MAs are designed to have a fixed frequency and the tunable MA [37–39] is now becoming a hot research field. If the absorption peaks of non-tunable MAs need to be changed to adapt to new application requirements, the geometric parameters of MA's must be carefully re-optimized. As mentioned above, the surface conductivity and E_F of BDSs can be dynamically tunable through alkaline surface doping or bias voltage. By changing the bias voltage of BDSs, the plasmonic resonant frequencies of the BDSs will be change.

Fig. 11(a). shows the absorption spectrum in different E_F (55–85 meV) of BDSs layer, and Fig. 11(b) is the corresponding scanning absorption spectrum. It can be seen from Fig. 11(a) that the tunable ability of the third absorption peaks is better than the first two absorption peaks, and the specific frequency adjustment information of the three absorption peaks are shown in Table 3. Therefore, the absorption peaks of MA can be adjusted by simply varying the bias voltage of BDSs.

Finally, the dependence of imaginary part k of the dielectric layer on the MA absorption spectrum is studied. Fig. 12 shows the simulation absorption spectrum in different k (0–0.09) of dielectric layer. From analyzing the absorption spectrum, the majority of THz radiation is

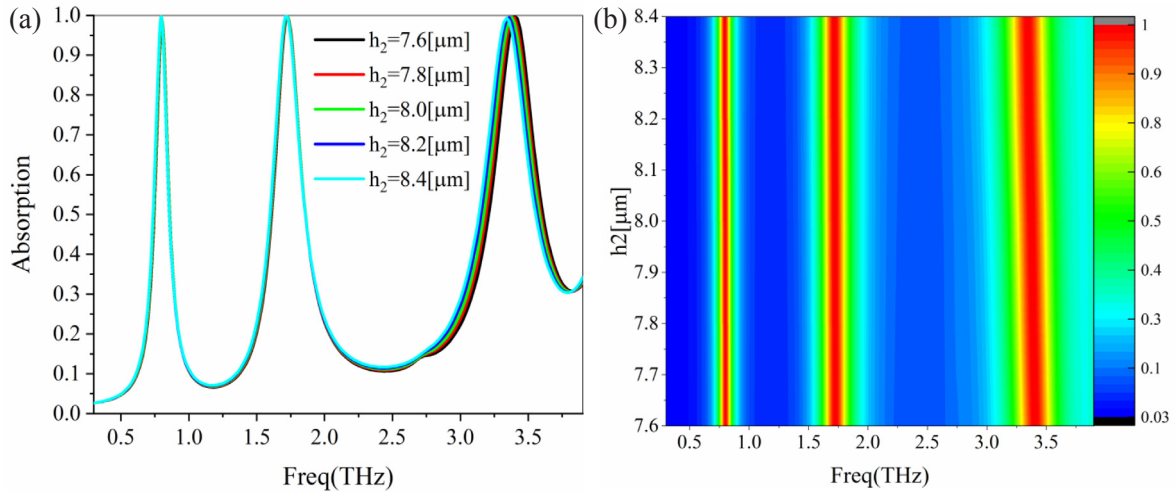

Fig. 9. (a) The absorption spectrum for different thickness of the dielectric layer, (b) The scanning absorption spectrum under different thickness of dielectric layer.

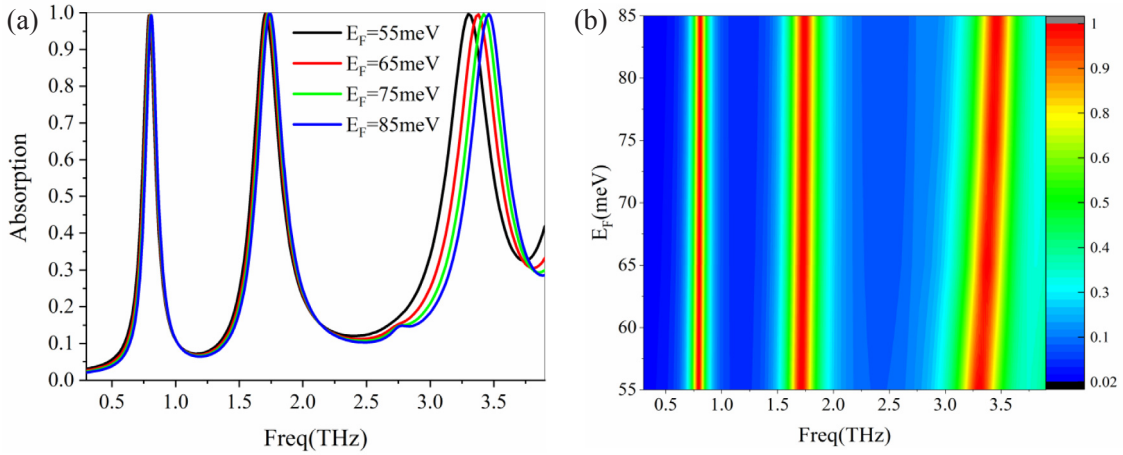

Fig. 11. (a) The absorption spectrum with different E_F (55–85 meV) of BDSs layer, (b) The scanning absorption spectrum under different E_F of BDSs layer.

Table 3
The peaks of MA in different E_F of BDSs.

(E_F)	Peak 1		Peak 2		Peak 3	
	Frequency (THz)	Absorbance	Frequency (THz)	Absorbance	Frequency (THz)	Absorbance
55 meV	0.79	99.33%	1.71	99.94%	3.30	99.68%
65 meV	0.80	99.43%	1.72	99.92%	3.38	99.58%
75 meV	0.805	99.41%	1.73	99.92%	3.42	99.62%
85 meV	0.81	99.32%	1.74	99.94%	3.46	99.65%

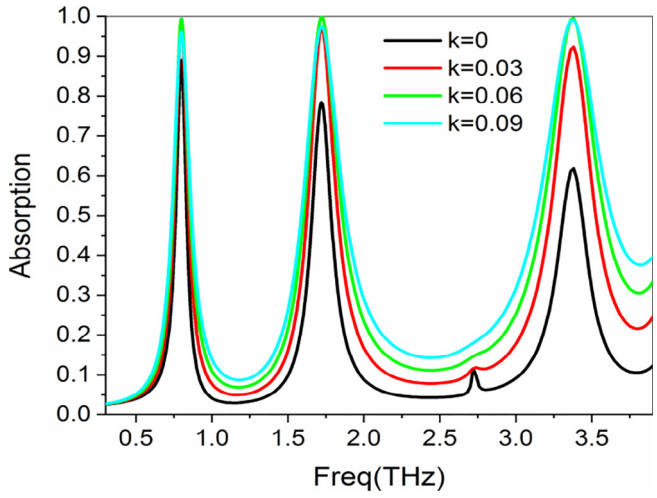

Fig. 12. The simulation absorption spectrum with different k (0–0.09) of dielectric layer.

absorbed by the absorption and BDSs layer as an oscillating electric current, and the rest of THz radiation is absorbed by the dielectric layer.

Conclusions

In this paper, a triple-band terahertz MA based on BDSs is proposed, which consists of a windmill-shaped element in a square ring layer, a dielectric layer and a BDSs layer. The MA unit cell is investigated at normal and oblique incidence angles for both TE and TM polarizations. The simulation results show that the MA has three high absorption peaks at 0.80 THz, 1.72 THz and 3.38 THz, and the corresponding absorbance are 99.43%, 99.92% and 99.58%, respectively. The absorption peaks of MA can be tuned by adjusting the E_F of the BDSs. The density of electric field, magnetic field and surface current distributions of the MA are also given to reveal the absorption mechanism. Furthermore, the numerical simulations is used to explain the relationships of the absorbance and the thickness of dielectric, incidence angle, E_F , and the imaginary parts of dielectric. The designed MA not only has high absorbance but also insensitive to polarizations, which is favorable for various applications, such as terahertz detecting, radar stealth and bio-chemical sensor.

Acknowledgements

This work was supported by the National Natural Science Foundation of China [Grant No. 61775027 and No. U1804165].

References

[1] Landy NI, Sajuyigbe S, Mock JJ, Smith DR, Padilla WJ. Perfect metamaterial absorber. Phys Rev Lett 2008;100.
[2] Watts CM, Liu X, Padilla WJ. Metamaterial electromagnetic wave absorbers. Adv Mater 2012;24(23):OP98–120.
[3] Ding F, Jin Y, Li B, et al. Ultrabroadband strong light absorption based on thin multilayered metamaterials. Laser Photonics Rev 2015;8(6):946–53.
[4] Ding F, Cui Y, Ge X, Jin Y, He S. Ultra-broadband microwave metamaterial absorber. Appl Phys Lett 2012;100:103506.
[5] Ghosh S, Bhattacharyya S, Kaiprath Y, Vaibhav Srivastava K. Bandwidth-enhanced polarization-insensitive microwave metamaterial absorber and its equivalent circuit model. J Appl Phys 2014;115:104503.
[6] Yi Z, Chen J, Cen C, Chen X, Zhou Z, Tang Y, et al. Tunable graphene-based plasmonic perfect metamaterial absorber in the THz region. Micromachines (Basel) 2019;10.
[7] Yi Z, Lin H, Niu G, Chen X, Zhou Z, Ye X, et al. Graphene-based tunable triple-band plasmonic perfect metamaterial absorber with good angle polarization-tolerance. Results Phys 2019;13:102149.
[8] Yi Z, Liu L, Wang L, Cen C, Chen X, Zhou Z, et al. Tunable dual-band perfect absorber consisting of periodic cross-cross monolayer graphene arrays. Results Phys 2019;13:102217.
[9] Liu N, Mesch M, Weiss T, Hentschel M, Giessen H. Infrared perfect absorber and its application as plasmonic sensor. Nano Lett 2010;10:2342–8.
[10] Li R, Wu D, Liu Y, Yu L, Yu Z, Ye H. Infrared plasmonic refractive index sensor with ultra-high figure of merit based on the optimized all-metal grating. Nanoscale Res Lett 2017;12:1.
[11] Li Z, Butun S, Aydin K. Large-area, lithography-free super absorbers and color filters

at visible frequencies using ultrathin metallic films. ACS Photonics 2015;2:183–8.
[12] Rahm M, Schurig D, Roberts DA, Cummer SA, Smith DR, Pendry JB. Design of electromagnetic cloaks and concentrators using form-invariant coordinate transformations of Maxwell's equations. Photonics Nanostruct Fundam Appl 2008;6:87–95.
[13] Costa F, Genovesi S, Monorchio A, Manara G. A circuit-based model for the interpretation of perfect metamaterial absorbers. IEEE Trans Antennas Propag 2013;61:1201–9.
[14] Bakır M, Karaaslan M, Unal E, Akgol O, Sabah C. Microwave metamaterial absorber for sensing applications. Opto-Electron Rev 2017;25:318–25.
[15] Rufangura P, Sabah C. Dual-band perfect metamaterial absorber for solar cell applications. Vacuum 2015;120:68–74.
[16] Li D, Huang H, Xia H, Zeng J, Li H, Xie D. Temperature-dependent tunable terahertz metamaterial absorber for the application of light modulator. Results Phys 2018;11:659–64.
[17] Darvishzadeh A, Alharbi N, Mosavi A, Gorji NE. Modeling the strain impact on refractive index and optical transmission rate. Physica B 2018;543:14–7.
[18] Wang BX, Wang GZ, Sang T. Simple design of novel triple-band terahertz metamaterial absorber for sensing application. J Phys D Appl Phys 2016;49(16):165307.
[19] Wang BX, Wang GZ, Sang T, et al. Six-band terahertz metamaterial absorber based on the combination of multiple-order responses of metallic patches in a dual-layer stacked resonance structure. Sci Rep 2017;7:41373.
[20] Iwaszczuk K, Strikwerda A, Fan K, Zhang X, Averitt R, Jepsen P. Flexible metamaterial absorbers for stealth applications at terahertz frequencies. Opt Express 2012;20:635–43.
[21] Xu R, Liu X, Lin Y-S. Tunable ultra-narrowband terahertz perfect absorber by using metal-insulator-metal microstructures. Results Phys 2019;13:102176.
[22] Wang B-X, Wang G-Z. Quad-band terahertz absorber based on a simple design of metamaterial resonator. IEEE Photonics J 2016;8:1–8.
[23] Zhang RX, Liu CX. Crystalline symmetry-protected majorana mode in number-conserving dirac semimetal nanowires. Phys Rev Lett 2018;120:156802.
[24] Chen H, Zhang H, Liu M, Zhao Y, Liu S, Zhang Y. Tunable multiple plasmon-induced transparency in three-dimensional Dirac semimetal metamaterials. Opt Commun 2018;423:57–62.
[25] Bolotin KI, Sikes KJ, Jiang Z, Klima M, Fudenberg G, Hone J, et al. Ultrahigh electron mobility in suspended graphene. Solid State Commun 2008;146:351–5.
[26] Wang Q, Wang X, Zhang L, Wang Y, Qiao W, Han X, et al. Tunable defect modes of one-dimensional photonic crystals containing a Dirac semimetal-based metamaterial defect layer. Appl Opt 2019;58:94–101.
[27] Liu GD, Zhai X, Meng HY, Lin Q, Huang Y, Zhao CJ, et al. Dirac semimetals based tunable narrowband absorber at terahertz frequencies. Opt Express 2018;26:11471–80.
[28] Chen H, Zhang H, Liu M, Zhao Y, Guo X, Zhang Y. Realization of tunable plasmon-induced transparency by bright-bright mode coupling in Dirac semimetals. Opt Mater Express 2017;7:3397.
[29] Meng WW, Lv J, Zhang L, Que L, Zhou Y, Jiang Y, et al. ultra-broadband and polarization-independent metamaterial absorber with bandwidth of 3.7 THz. Opt Commun 2019;431:255–60.
[30] Pan W, Yu X, Zhang J, Zeng W. A broadband terahertz metamaterial absorber based on two circular split rings. IEEE J Quantum Electron 2017;53:1–6.
[31] Wang B-X, Wang G-Z, Wang L-L. Design of a novel dual-band terahertz metamaterial absorber. Plasmonics 2015;11:523–30.
[32] Kotov OV, Lozovik YE. Dielectric response and novel electromagnetic modes in three-dimensional Dirac semimetal films. Phys Rev B 2016;93.
[33] Sushkov AB, Hofmann JB, Jenkins GS, Ishikawa J, Nakatsuji S, Das Sarma S, et al. Optical evidence for a Weyl semimetal state in pyrochloreEu2Ir2O7. Phys Rev B 2015;92.
[34] He X, Yao Y, Zhu Z, Chen M, Zhu L, Yang W, et al. Active graphene metamaterial absorber for terahertz absorption bandwidth, intensity and frequency control. Opt Mater Express 2018;8:1031.
[35] Huang H, Xia H, Xie W, Guo Z, Li H, Xie D. Design of broadband graphene-metamaterial absorbers for permittivity sensing at mid-infrared regions. Sci Rep 2018;8:4183.
[36] Smith DR, Vier DC, Koschny T, Soukoulis CM. Electromagnetic parameter retrieval from inhomogeneous metamaterials. Phys Rev E Stat Nonlin Soft Matter Phys 2005;71:036617.
[37] Mu H, Yong C, Zheng C, et al. Design of a broadband tunable terahertz metamaterial absorber based on complementary structural graphene. Materials 2018;11(4):540–9.
[38] Yong C, Mu H, Hao C, et al. Ultrathin six-band polarization-insensitive perfect metamaterial absorber based on a cross-cave patch resonator for terahertz waves. Materials 2017;10(6):591–603.
[39] Cheng Y, Gong R, Cheng Z. A photoexcited broadband switchable metamaterial absorber with polarization-insensitive and wide-angle absorption for terahertz waves. Opt Commun 2016;361:41–6.